Theta- and gamma-band oscillatory uncoupling in the macaque hippocampus

S. Abbaspoor[1], A.T. Hussin[2], and K.L. Hoffman[1,2]

Affiliations:

[1] Department of Psychology, Vanderbilt Vision Research Center, Vanderbilt Brain Institute, Vanderbilt University, Nashville, Tennessee

[2] Department of Biology, Center for Vision Research, York University

Abstract

Nested hippocampal oscillations in the rodent gives rise to temporal coding that may underlie learning, memory, and decision making. Theta/gamma coupling in rodent CA1 occurs during exploration and sharp-wave ripples during quiescence. Whether these oscillatory regimes extend to primates is less clear. We therefore sought to identify correspondences in frequency bands, nesting, and behavioral coupling taken from macaque hippocampus. We found that, in contrast to the rodent, theta and gamma frequency bands in macaque CA1 were segregated by behavioral states. Beta/gamma (15-70Hz) had greater power during visual search while theta (7-10 Hz) dominated during quiescence. Moreover, delta/theta (3-8 Hz) amplitude was strongest when beta2/slow gamma (20-35 Hz) amplitude was weakest, though the low frequencies coupled with higher, ripple frequencies (60-150 Hz). The distribution of spike-field coherence revealed three peaks matching the 3-10 Hz, 20-30 Hz and 60-150 Hz bands; however, the low frequency effects were primarily due to sharp-wave ripples. Accordingly, no intrinsic theta spiking rhythmicity was apparent. These results support a role for beta2/slow gamma modulation in CA1 during active exploration in the primate that is decoupled from theta oscillations. These findings diverge from the rodent oscillatory canon and call for a shift in focus and frequency when considering the primate hippocampus.

Introduction

Hippocampal oscillations are heralded as canonical examples of how oscillations may give rise to behavioral and cognitive phenomena by coordinating information processing in neural circuits (1–4). In turn, behavioral states and patterns constrain and entrain specific neural oscillations. In rodents, locomotion and other exploratory movements elicit an ~8 Hz theta oscillation in hippocampal CA1, (5–8) and a faster gamma oscillation 25-100 Hz that nests within theta (2,9–11). In contrast, during quiescent states, theta and gamma oscillations are suppressed and sharp-wave ripple complexes emerge, the latter consisting of large high-frequency oscillations (150-250 Hz) in CA1 that occur within a slower (sharp-wave) deflection (12,13). Although the occurrence of sharp wave ripples during quiescence is highly conserved across species (12), its dichotomy with theta is less clear (14,15). This may stem from differences in how and when theta oscillations appear across phylogenetic order (16,17), particularly among primates (17–23). Consequently, gamma-coupling to theta (2,10,24), and the presence – as postulated – of sub-bands of gamma (2,11,25,26), could understandably be affected by the scarcity of theta oscillations in primates during species-relevant exploration (15,21,22,27,28). In the present study, we therefore adopted a hypothesis-generating (data-driven) approach to identify i. which oscillatory bands emerge in macaque hippocampal CA1 as a function of behavioral state; ii. whether these oscillations coalesce or compete, and iii. to what extent local single units are modulated at these rhythms.

Results and Discussion

Spectral analysis of hippocampal LFP during active search and quiescence

We recorded 42 sessions (LE: 26 sessions, LU: 16 Sessions) in the hippocampal CA1 subfield of two macaques during active visual search and quiescence (henceforth: ‘rest’). Consistent with previous reports (15,29), we observed bouts of roughly 20-30 Hz oscillations predominantly during search, and slower-frequency, larger-amplitude local field potentials (LFPs) during rest (Fig. 1A, C). To visualize the relationship between spectral power across frequency bands, we sorted quantiles of 1.024-s segments based on their average power in the 20-30 Hz frequency band, revealing an antagonistic relationship between 20-30 Hz and <10 Hz frequencies (Fig. 1B) i.e. when power at 20-30 Hz was greatest, <10 Hz power was qualitatively weakest. In contrast, stronger power at <10 Hz was accompanied by stronger power at >60 Hz. To determine whether the spectrum varies with behavioral epoch, as it does in rodents (5,30,31), we calculated the power spectrum for each behavioral state (Fig. 1D). To disentangle the estimated oscillatory power of brain signals from its 1/f background component (32–35) we created aperiodic-adjusted power

spectra as described in 33), which showed a stronger 7-10 Hz power during rest compared to active search (Fig. 1D, Middle). In contrast, power in the higher frequencies from 15-70 Hz was stronger during active search compared to rest, with a peak in the 20-30 Hz range (both, $p<0.05$ Wilcoxon signed rank test with FDR correction). These spectral-behavioral correlates are in stark contrast to those seen in rats and mice, leading to the question of whether theta and the beta/slower gamma frequencies couple, as they commonly do in rodents (10,36–38).

Hippocampal cross-frequency coupling

To measure the coupling of oscillations, we first computed cross-frequency power correlations across the spectrum. Consistent with the qualitative pattern shown in Fig. 2B, power at 3-8 Hz and 20-35 Hz were negatively correlated (Fig. 1E, $p<0.05$ using a cluster-based permutation test corrected for multiple comparisons). The 20-35 Hz range is therefore unlikely to be a result of harmonics of the slower 8 Hz oscillation, as has been found in rodent hippocampal oscillations (39); however, the 20-35 Hz band may give rise to its own ~50 Hz harmonic, apparent in Fig. 1A-E. In addition, power in the slower, 3-8 Hz band was positively correlated with that of a much faster, 80-150 Hz band.

To estimate phase-amplitude coupling in the LFP, we performed bicoherence analysis, (Fig. 1F; (40–42), revealing a peak cluster around the 25 Hz frequency range which confirms an interaction between the activity at this frequency and its second harmonic. In addition, the 3-8 Hz band was coupled to high frequencies of 95-150 Hz ($p<0.05$, cluster-based Monte Carlo statistical test). This is consistent with our power-power coupling results and indicates that the correlated envelopes in Fig. 1E are driven by phase-specific coupling of the high frequencies (Fig. 1B). The caveat to using the term “phase amplitude coupling”, is that aperiodic low frequencies can give spurious “coupling” to the amplitude of high frequencies (41–44), as demonstrated with sharp-wave phase modulation of ~3Hz that can produce an artifactual ‘theta’ component in comodulograms (15,45,46).

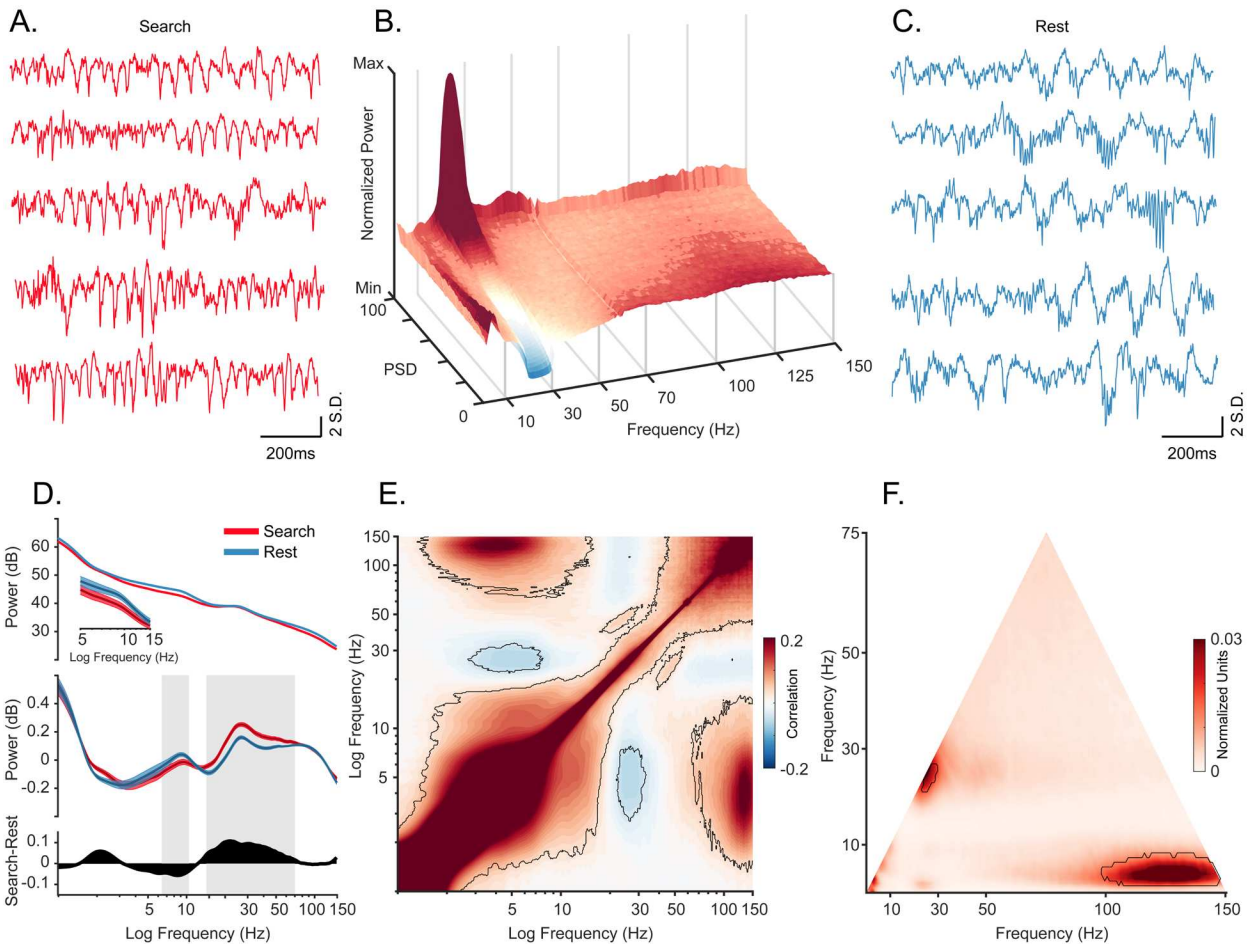

Figure 1. Oscillatory decoupling in CA1 field potentials. A. Example traces of wideband LFP in CA1 during search. Data segments were taken from epochs with characteristic high 20-30 Hz power, shown in B (traces were linearly detrended for visualization). **B.** Spectral density sorted by 20-30 Hz power. Surface plot shows data segments sorted into quantiles according to 20-30 Hz power, revealing an apparent increase in 5-10 Hz power when 20-30 Hz power is weakest. See Methods for details. **C.** Example traces of wideband LFP in CA1 during the rest epoch showing characteristic interactions between <10 Hz and >60 Hz oscillations. Conventions as in A. **D.** ***Top.*** Mean power spectral density during search (red), and rest (blue). *Inset*: mean power for low frequencies of main plot, with shaded 95% bootstrap confidence interval (N=42 sessions). ***Middle.*** Power spectral density after fitting and subtracting the aperiodic 1/f component during search and rest, with shaded 95% bootstrap confidence intervals. Gray areas show significant differences in power across behavioral epochs ($p<0.05$, Wilcoxon signed rank test, FDR corrected) ***Bottom.*** Power difference between search and rest. **E.** Average cross-frequency power comodulogram (N=42 sessions). Dark outline represents areas that were significant in at least 80% of samples ($p < 0.05$, cluster-based permutation test corrected for multiple comparisons). **F.** Average bicoherence of the CA1 LFP (N=42 sessions). Dark outline represents areas that were significant in at least 80% of samples ($p < 0.05$, Monte Carlo test corrected for multiple comparisons).

Oscillatory modulation of spiking activity

Spectral peaks do not necessarily indicate the presence of an oscillation in the underlying neural activity (26,47,48). If an oscillatory pattern is present in the local neural population, regular comodulation between spikes and the field oscillation phase should occur. We measured the spike-field coherence by calculating pairwise phase consistency (49) for well-isolated units (N=404). Individual cells phase locked to multiple frequencies (Fig. 2A; $p<0.05$, permutation test and Rayleigh test $p<0.05$), with the population showing the full range of spike preferred frequencies of modulation (Fig. 2C).

Given the weaker power at 7-10 Hz during active search, and the strong coupling between bands at 3-8 Hz and >95 Hz, we hypothesized that spike-LFP coherence at low frequencies might be produced as a byproduct of the slow component of sharp-wave ripples (SWRs) (14) rather than via true oscillations. To test this, we extracted peri-SWR spikes, computed PPC only for these spikes in each cell [PPC_{swr}], and then compared this to the PPC for spikes outside the SWR window [$PPC_{residual}$]. Fig. 2B shows a cell that exhibits stronger spike-LFP coherence at 8 Hz during SWR than outside the SWR window ($p<0.05$, permutation test with FDR correction). The majority of cells at lower frequencies (2-10 Hz) had a greater coherence during the SWR. In contrast, for a majority of the cells, the spike-field coherence decreased for higher frequencies (10-200Hz) during SWRs (Fig. 2D). This led to weaker mean spike-field coherence restricted to the “theta” < 10 Hz range, after removing the influence of SWRs, suggesting a contribution of the non-oscillatory slow deflection in the SWR complex to the apparent “cross-frequency” interactions.

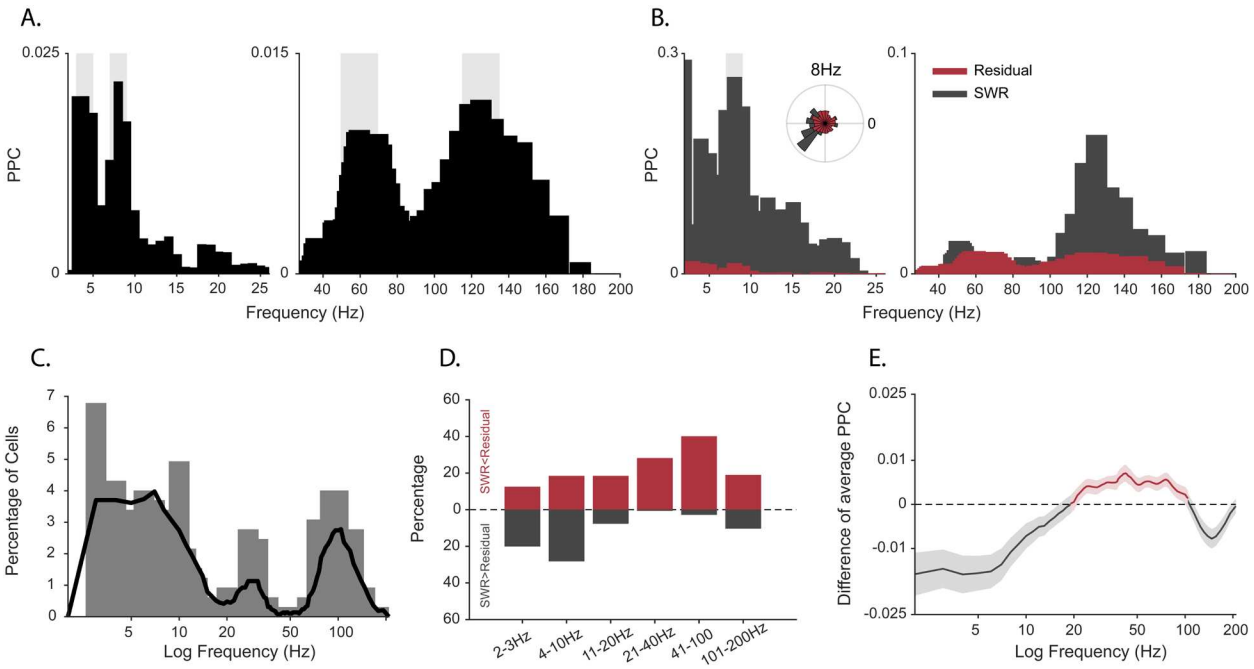

Figure 2. Spike-field coherence and its influence by sharp-wave ripples. A. Spike-LFP Pairwise phase consistency (PPC) spectra for an example unit. Shaded gray shows significant values ($p<0.05$, permutation test and Rayleigh test $p<0.05$). **B.** Spike-LFP coherence for spikes during detected SWRs (dark gray) and residual LFP after removing the SWR contributions (red). Light gray shading shows significant difference at $p < 0.05$ in FDR-corrected permutation test for the SWR group. Inset: Normalized histogram of the phase values at 8 Hz, obtained from the spike-LFP coherence analysis shown in A. **C.** Distribution of the maximum preferred PPC frequency across units, before adjusting for SWRs (N = 404 units). **D.** Difference in the proportion of cells with greater spike-LFP coherence for SWR (grey) and SWR-removed residual (red), for 4 frequency bands (N=185 units). **E.** SWR-residual difference of mean Spike-LFP coherence. Shading shows 95% bootstrapped confidence interval. Positive values indicating greater PPC for residual than SWR groups are shown in red, negative values (SWR>residual) in dark gray.

Given the methods available in this study, the strongest demonstration of oscillations within local circuits would be periodic spiking of single units. For example, theta modulation is regular and robust when measured as periodic peaks of the spike autocorrelograms of rats and mice (~8Hz, Fig. 3A, C from homologous subregions of CA1; (50–52). Qualitative visual inspection failed to reveal any clear theta-locked cells in the spike autocorrelogram, similar to findings in marmosets and humans (22,53). Fig. 3A shows the autocorrelogram of the example spike-field coupled cell in Fig. 2A overlaid on top of a theta rhythmic cell from the homologous CA1 region of a rat (i.e. temporal CA1). To quantify theta autocorrelogram rhythmicity we calculated theta modulation index (52). Compared to modulations seen in the rat (Fig. 3B in gray), our cells typically showed near zero index values i.e. low to no modulation (Fig. 3B in black), which was also evident in the sorted-cell and mean population autocorrelogram (Fig. 3C). Higher frequencies are less likely to demonstrate cycle-by-cycle periodicity due to their shorter periods, nevertheless, we observed

157 protracted >20 Hz spike modulation in the spike triggered averages and autocorrelograms of
158 several cells (Fig. 4).

159

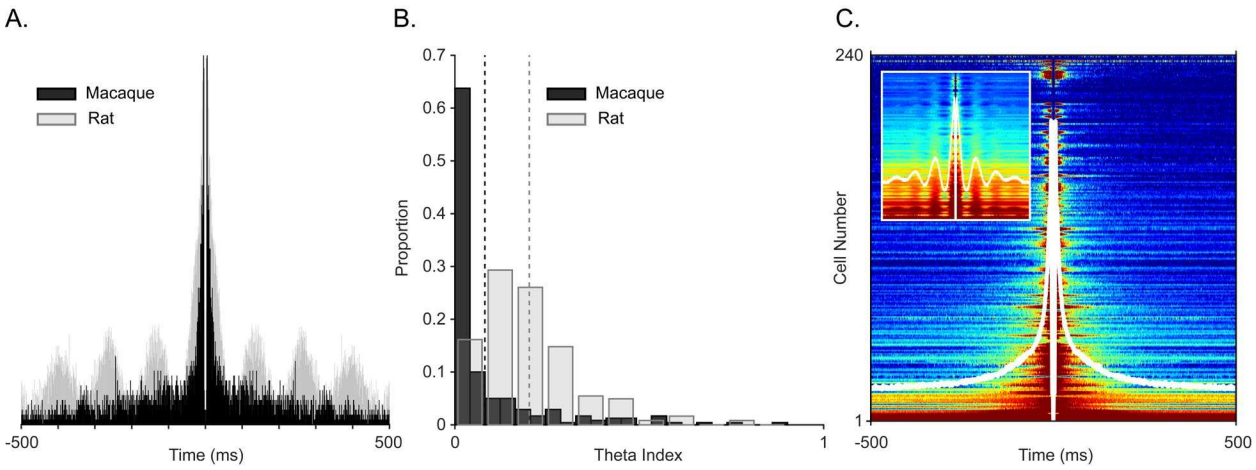

160

161 **Figure 3. Examining spiking periodicity for theta modulation in macaque hippocampus**. **A.** Autocorrelogram of
162 an example "theta" unit from Figure 2A (black, N= 945 total spikes) and a theta-modulated unit in rat (grey, N= 5655
163 total spikes). **B.** Distribution of the theta index in CA1 units from this study (black, N=240 units), and CA1 units of rat
164 (gray, N=197 units). Dashed lines show mean values, color coded by species. **C.** Sorted autocorrelograms of CA1
165 units, with mean, population ACG shown as a white trace. Inset: same as the main plot but for rats.

166

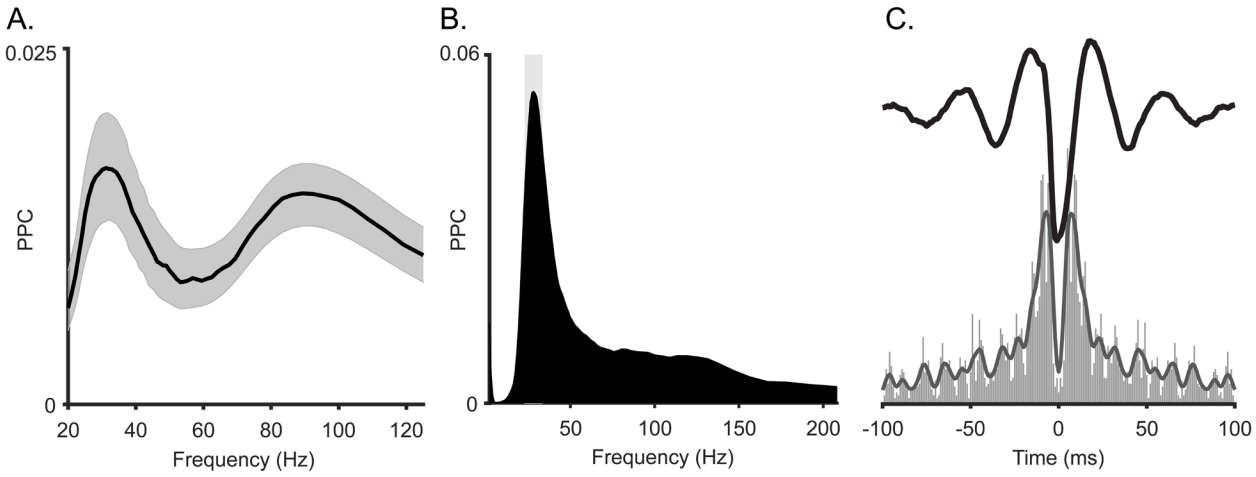

167

168 **Figure 4. Spike-LFP coherence of the slow gamma oscillation in macaque hippocampus**. **A.** Average spike-LFP
169 coherence in gamma frequency range. Shading shows 95% bootstrap confidence interval. **B.** Spike-LFP coherence for
170 a representative gamma-locked unit. This unit had a significant peak at 30Hz ($p<0.05$, permutation test and Rayleigh
171 test $p<0.05$). **C. Top:** Spike-triggered average LFP of the unit in B. **Bottom**: Autocorrelogram of the same unit, with
172 Gaussian smoothing.

Conserved and distinct oscillations in primates

Despite multiple independent generators of theta observed in rats and mice (8,54–56), both bat and primate hippocampal regions appear to have a distinct brain-behavioral coupling to theta (16,19,21,23,57–59). This extends to the high-arousal state of locomotion, at least when recording locally, from the hippocampus proper in monkeys (21,22,60). At the other arousal extreme, sleep stages in rodents (NREM and REM) are known to show a parallel dichotomy between SWRs and theta, respectively (7,61–63). Here, again, well-localized CA1 recordings in macaques reveal heightened theta power during quest wakefulness and/or NREM and greater beta/slow gamma in REM sleep, in apparent dissociation by arousal state (20,64). These results, which match closely our findings during exploratory behaviors, are also apparent in the depth-electrode sleep recordings in humans (18,65–67) but stand in contrast to the canonical oscillations of rodents. During waking and cognitive tasks in humans, the results using depth electrodes in the medial temporal lobe are varied (see reviews (23,48)), and therefore more difficult to compare across primate species, method, task, and result. The decoupling of some bands or generators of the beta2/slow gamma from theta, however, may ultimately prove to be conserved across species (68,69).

As it currently stands, our findings offer a hypothesis-generating framework for future analysis in (human and non-human) primate hippocampal physiology. The present results suggest that theta oscillations were not prevalent during search in primates and did not consistently modulate single unit activity. Instead, ~20-30 Hz “slow gamma” oscillations constitute the chief, self-contained oscillation that arises during active exploration in the primate hippocampus and stands as the most likely oscillation for organizing local information processing during exploration.

Methods

Subjects and task

All procedures were conducted with approval from the local ethics and animal care authorities (Animal Care Committee, Canadian Council on Animal Care). Two adult female macaques (*Macaca mulatta*) were used in this study, and data from these experiments have been reported previously (14,15,29,70). The apparatus, training procedure, and task, described previously (15,71), and described briefly here. During search, animals performed a hippocampally-dependent visual target-detection task. In the task, monkeys were required to identify a target object from nontargets in unique visual scenes and report their selection of scene-unique target objects by holding their gaze on the target region for a prolonged (≥800 ms) duration. Target objects were defined as a changing item in a natural scene image, where the original and changed images were presented in alternation, each lasting 500 ms, with a brief grey-screen (50 ms) shown between image presentations. An inter-trial interval (ITI) of 2–20 s followed each trial. The daily sessions began and ended with a period of at least 10 min when no stimulus was presented within the darkened booth and animals could sleep or sit quietly ('rest').

Electrophysiological recordings

Bundles of moveable platinum/tungsten multicore tetrodes (96 µm outer diameter; Thomas Recordings) were implanted into the anterior half of hippocampus and lowered into CA1. Recording sites were verified with postoperative CT co-registered to pre-operative MRI and using functional landmarks that changed with depth during lowering, as described in the previous studies. Post-explant MRI verified the bundle location in one animal (15). For the current study, we detected channels within the pyramidal layer based on the strongest amplitude of ripples during SWRs and single unit activity, and only used these channels for all analyses.

LFPs were digitally sampled at 32 kHz using a Digital Lynx acquisition system (Neuralynx, Inc.) and filtered between 0.5 Hz and 2 kHz. Single-unit activity was sampled at 32 kHz and filtered between 600 Hz and 6 kHz, recording the waveform for 1 ms around a threshold triggered spike events. Spike sorting was performed semi-automatically using KlustaKwik based on wave shape, principal components, energy, and peak/valley across channels. This was followed by manual curation of clusters in MClust (A.D. Redish).

Sharp wave ripple detection

Sharp wave ripples (SWR) detection was performed on the tetrode channel with the most visibly apparent ripple activity using the previously described method (15). Raw LFPs recorded from the tetrode channel were filtered between 100-250 Hz. To determine the SWR envelope, filtered LFPs were transformed into z-scores and rectified and subjected to a secondary band-pass filter between 1-20 Hz. Events with a minimum amplitude exceeding 3 SDs above the mean with a minimum duration of 50 ms, beginning and ending at 1 SD were designated as potential ripples. High frequency energy is present for non-SWR events such as EMG and other non-biological noise, though these artifacts are distinct from ripples because the latter are restricted to the regions near the pyramidal layer. For artifact (non-ripple-event) rejection, a distant tetrode channel was selected as a 'noise detecting' channel. Events that were concurrently detected on the noise channel and the 'ripple-layer' channel were removed from the ripple pool.

Power Spectral Parametrization and Fitting

To compare the spectral content during search and rest, we selected successfully completed trials lasting longer than 1 second. For rest trials, we extracted the LFP signals that were recorded before the start of the task and after the end of the task when the animal was in a dark environment in a quiescent or inactive state. We used Welch's method with a 50%-overlapping 1024-sample sliding Hanning window to estimate power spectra for the frequency range of 1 to 150 Hz with a frequency resolution of 0.25 Hz.

To identify spectral peaks and compare between search and rest states, we parameterized power spectra using the method described by (33). This method models power spectra as a combination of the 1/f frequency components (aperiodic) in addition to a series of Gaussians that capture the presence of peaks (periodic components). The model was fit to a frequency range between 1 to 200 Hz with a frequency resolution of 0.5 Hz. Settings for the algorithm were set as: peak width limits: (0.5, 12); max number of peaks: infinite; minimum peak height: 0; peak threshold: 2.0; and aperiodic mode: 'Fixed'.

To assess statistical significance for the difference in parametrized spectra at each frequency, we used Wilcoxon signed rank test at $p < 0.05$ with FDR correction for multiple comparisons.

20-30 Hz sorted spectral density map:

We estimated the power spectral density using Welch's method described in the previous section to obtain (frequency * PSD segments) matrix. We then sorted the PSD segments based on the mean power in 20-30 Hz frequency range and normalized each segment by dividing it by its median. We clustered all sorted segments into 50 total segments of equal size (frequency * 50 segments) by averaging original PSD sorted segments. We repeated this procedure across sessions and animals separately.

Cross-frequency Power Correlation

On continuous LFP time-series data, Welch's method with a 50%-overlapping 1024-sample sliding Hanning window was used to estimate the spectrogram for the frequency range of 1 to 150 Hz with a frequency resolution of 0.25 Hz.

We computed the pairwise correlation between cross-frequency power using the following formula (72):

$$corr_{ij} = \frac{\sum_k (S_k(f_i) - \overline{S(f_i)})(S_k(f_j) - \overline{S(f_j)})}{\sigma_i \sigma_j}$$

where $S_k(f_i)$ is the PSD at the frequency f_i in time-window k, $\overline{S(f_i)}$ the averaged PSD at the frequency f_i overall sliding window, σ_i the standard deviation of the PSD at the frequency f_i, and k ranges over all sliding windows.

To test the null hypothesis that the power spectral time series of two different frequencies, f_i and f_j , are not coupled in the data, we performed a non-parametric surrogate data method with cluster-based multiple comparison correction (73). This method preserves the original data's statistical properties while generating time series that are randomized such that any possible nonlinear coupling is removed. In this method, we randomized time-window k differently for each frequency bin to build surrogate time-frequency time series' and computed the surrogate cross-frequency power correlation. This process was repeated 5000 times to produce distributions for the dataset in which the null hypothesis holds. The original, non-permuted data are then compared to the surrogate distribution to obtain uncorrected p-values. The significance threshold was selected to be 0.05. For cluster-based multiple comparison correction, all samples were selected whose p-value was smaller than 0.05. Selected samples were then clustered in

connected sets based on their adjacency and the cluster size was calculated. This procedure was performed 5000 times to produce the distribution of cluster sizes. If cluster sizes in the original correlation matrix were larger than the cluster threshold at 95-th quantile, they were reported as significant. We performed this statistical procedure at the level of single channels per animal. We consider as robust significance those areas that were significant for at least 80% of all samples.

Bicoherence

For Bicoherence, we used the HOSA toolbox. Bicoherence was estimated for frequencies f_1 (1 to 75 Hz) and f_2 (1 -150 Hz) in steps of 1 Hz according to the following formula (74):

$$B(f_1, f_2) = \frac{|\langle F_t(f_1)F_t(f_2)F_t^*(f_1+f_2)\rangle_t|}{\langle|F_t(f_1)F_t(f_2)F_t^*(f_1+f_2)|\rangle_t}$$

Where $F_t(f)$ is the signal's time-frequency transformation at time t, | | represents the absolute value, and ⟨ ⟩ is the average over time. We set the segment length to 1024 samples for this analysis.

Bicoherence has a higher spectral resolution for disentangling harmonic from non-harmonic cross-frequency coupling. Additionally, bicoherence relaxes the artificial spectral constraints introduced by conventional PAC, corrects for its poor biases, and accounts for asymmetry in the rhythms (40,42,75).

Theoretically, the bispectrum is statistically zero for linear systems with mutually independent Fourier coefficients. For nonlinear systems, the bispectrum will exhibit peaks at triads (f_n, f_m, f_{n+m}) that are phase correlated, measuring the degree of three-wave coupling (75). In practice, however, bicoherence has a positive bias The background activity of LFP signals can be estimated by properties of red noise which can then be used for significance testing (76,77). To calculate the statistical significance of local autobicoherence, we generated red noise with the same length of our original signals and computed Bicoherence for each red noise. We repeated this procedure 5000 times to obtain the null distribution. We then compared the original data to the null distribution to obtain uncorrected p-values, thresholded for significance at 0.05. We then performed multiple comparison corrections as described earlier in the text.

Spike-Field Synchronization:

To quantify spike-field synchronization, we used fieldtrip toolbox (MATLAB) to compute pairwise phase consistency (PPC) which is unbiased by the number of spikes (49). Raw continuous recordings were resampled with a 1000 Hz sampling rate. The spectral content was estimated with a frequency-dependent Hanning window with 5 cycles per frequency and frequency resolution of 1Hz. All detected spikes of a unit during the session were included. To assess the statistical significance of spike-field synchronization, we first used a non-parametric permutation test with minimal assumptions. In this procedure, the distribution of PPC values was estimated from 1000 iterations of shuffled spike times of each cell. We used the PPC distribution of shuffles to compute the PPC threshold for significance at each frequency. We applied a threshold of uncorrected $p < 0.05$ to determine the significant synchronization at each frequency. Only PPC values that exceeded the statistical threshold and had a Rayleigh test $p<0.05$ and a minimum peak and peak prominence of 0.005 were reported as significant.

To compare spike-field synchronization during SWRs, we extracted spikes inside a 600ms window centered around the SWR events and computed PPC [PPC_{SWR}]. These spikes were then excluded from the unit spike timestamps and PPC was calculated for the remaining 'residual' spikes [$PPC_{residual}$]. PPC_{SWR} was then compared with $PPC_{residual}$. Only cells with at least 20 spikes during ripple time windows were included in this analysis.

To test the significance of differences in spike-field coupling within SWR epochs or excluding them, on a per-unit basis, spikes were randomly selected and assigned to SWR and residual conditions. In this random selection, spike counts were controlled to correspond to the original condition. We performed the random selection 1000 times and measured the difference between PPC in each iteration to obtain the null distribution. Then, we grouped frequencies into 5 bands 2-3, 4-10, 11-20, 21-40, 41-100, 101-200 Hz. In each frequency band, we found the peak frequency at which the absolute PPC difference was largest and only tested these for significance. If the p-value of PPC difference was less than 0.05 (two-tailed) after FDR correction, it was labeled as significant.

Theta modulation index (TMI) Estimation

We used the 52) method to quantify the degree of theta modulation in single units. For all units, we first computed the autocorrelogram of the cell, in 10 ms bins from -500 to +500 ms, normalized

to the maximum value between 100 and 150 ms (corresponding to theta modulation), and clipped all values above 1. We only included autocorrelograms with at least 100 counts for further steps (N=240 units). We then fit each autocorrelogram with the following function:

$$y(t) = [a(sin(\omega t) + 1) + b] * e^{-|t|/\tau_1} + c * e^{-t^2/\tau_2^2}$$

Where t is the autocorrelogram time lag from -700 to 700ms, and $a - c$, ω, and τ_{1-2} were fit using the $fminsearch$ optimization function in MATLAB. The theta indexes were defined as the ratio of the fit parameters a/b. For best-fitting performance, we restricted possible values for ω to (4, 10), for a and b to non-negative values, for c to (0, 0.2), and for τ_2 to (0, 0.05).

Additional single unit datasets

To generate example plots of theta rhythmic cells (Fig. 3), recordings from the Buzsáki laboratory were included (https://buzsakilab.nyumc.org/datasets/RoyerS/).

Acknowledgements

The authors wish to thank A. Maurer for thoughtful comments on the manuscript. This work was funded by the Krembil Foundation, Brain Canada, NSERC, and the Whitehall Foundation.

Bibliography

1. Klausberger T, Somogyi P. Neuronal diversity and temporal dynamics: the unity of hippocampal circuit operations. Science. 2008 Jul 4;321(5885):53–7.

2. Colgin LL. Rhythms of the hippocampal network. Nat Rev Neurosci. 2016 Apr;17(4):239–49.

3. Buzsáki G, Draguhn A. Neuronal oscillations in cortical networks. Science. 2004 Jun 25;304(5679):1926–9.

4. Hahn G, Ponce-Alvarez A, Deco G, Aertsen A, Kumar A. Portraits of communication in neuronal networks. Nat Rev Neurosci. 2019 Feb;20(2):117–27.

5. Whishaw IQ, Vanderwolf CH. Hippocampal EEG and behavior: changes in amplitude and frequency of RSA (theta rhythm) associated with spontaneous and learned movement patterns in rats and cats. Behav Biol. 1973 Apr;8(4):461–84.

6. Kramis R, Vanderwolf CH, Bland BH. Two types of hippocampal rhythmical slow activity in both the rabbit and the rat: relations to behavior and effects of atropine, diethyl ether, urethane, and pentobarbital. Exp Neurol. 1975 Oct;49(1 Pt 1):58–85.

7. Vanderwolf CH. Hippocampal electrical activity and voluntary movement in the rat. Electroencephalogr Clin Neurophysiol. 1969 Apr;26(4):407–18.

8. Buzsáki G. Theta oscillations in the hippocampus. Neuron. 2002 Jan 31;33(3):325–40.

9. Colgin LL, Moser EI. Gamma oscillations in the hippocampus. Physiology (Bethesda). 2010 Oct;25(5):319–29.

10. Bragin A, Jandó G, Nádasdy Z, Hetke J, Wise K, Buzsáki G. Gamma (40-100 Hz) oscillation in the hippocampus of the behaving rat. J Neurosci. 1995 Jan;15(1 Pt 1):47–60.

11. Csicsvari J, Jamieson B, Wise KD, Buzsáki G. Mechanisms of gamma oscillations in the hippocampus of the behaving rat. Neuron. 2003 Jan 23;37(2):311–22.

12. Buzsáki G. Hippocampal sharp wave-ripple: A cognitive biomarker for episodic memory and planning. Hippocampus. 2015 Oct;25(10):1073–188.

13. Ylinen A, Bragin A, Nádasdy Z, Jandó G, Szabó I, Sik A, et al. Sharp wave-associated high-frequency oscillation (200 Hz) in the intact hippocampus: network and intracellular mechanisms. J Neurosci. 1995 Jan;15(1 Pt 1):30–46.

14. Hussin AT, Leonard TK, Hoffman KL. Sharp-wave ripple features in macaques depend on behavioral state and cell-type specific firing. Hippocampus. 2018 Oct 29;

15. Leonard TK, Mikkila JM, Eskandar EN, Gerrard JL, Kaping D, Patel SR, et al. Sharp Wave Ripples during Visual Exploration in the Primate Hippocampus. J Neurosci. 2015 Nov 4;35(44):14771–82.

16. Ulanovsky N, Moss CF. Hippocampal cellular and network activity in freely moving echolocating bats. Nat Neurosci. 2007 Feb;10(2):224–33.

17. Green JD, Arduini AA. Hippocampal electrical activity in arousal. J Neurophysiol. 1954 Nov;17(6):533–57.

18. Halgren E, Babb TL, Crandall PH. Human hippocampal formation EEG desynchronizes during attentiveness and movement. Electroencephalogr Clin Neurophysiol. 1978 Jun;44(6):778–81.

19. Stewart M, Fox SE. Hippocampal theta activity in monkeys. Brain Res. 1991 Jan 4;538(1):59–63.

20. Tamura R, Nishida H, Eifuku S, Fushiki H, Watanabe Y, Uchiyama K. Sleep-stage correlates of hippocampal electroencephalogram in primates. PLoS ONE. 2013 Dec 30;8(12):e82994.

21. Talakoub O, Sayegh PF, Womelsdorf T, Zinke W, Fries P, Lewis CM, et al. Hippocampal and neocortical oscillations are tuned to behavioral state in freely-behaving macaques. BioRxiv. 2019 Feb 18;

22. Courellis HS, Nummela SU, Metke M, Diehl GW, Bussell R, Cauwenberghs G, et al. Spatial encoding in primate hippocampus during free navigation. PLoS Biol. 2019 Dec 9;17(12):e3000546.

23. Jacobs J. Hippocampal theta oscillations are slower in humans than in rodents: implications for models of spatial navigation and memory. Philos Trans R Soc Lond B Biol Sci. 2014 Feb 5;369(1635):20130304.

24. Lisman JE, Jensen O. The θ-γ neural code. Neuron. 2013 Mar 20;77(6):1002–16.

25. Colgin LL, Denninger T, Fyhn M, Hafting T, Bonnevie T, Jensen O, et al. Frequency of gamma oscillations routes flow of information in the hippocampus. Nature. 2009 Nov 19;462(7271):353–7.

26. Buzsáki G, Wang X-J. Mechanisms of gamma oscillations. Annu Rev Neurosci. 2012 Mar 20;35:203–25.

27. Hoffman KL, Dragan MC, Leonard TK, Micheli C, Montefusco-Siegmund R, Valiante TA. Saccades during visual exploration align hippocampal 3-8 Hz rhythms in human and non-human primates. Front Syst Neurosci. 2013 Aug 30;7:43.

28. Jutras MJ, Fries P, Buffalo EA. Oscillatory activity in the monkey hippocampus during visual exploration and memory formation. Proc Natl Acad Sci USA. 2013 Aug 6;110(32):13144–9.

29. Leonard TK, Hoffman KL. Sharp-Wave Ripples in Primates Are Enhanced near Remembered Visual Objects. Curr Biol. 2017 Jan 23;27(2):257–62.

30. Buzsáki G. The hippocampo-neocortical dialogue. Cereb Cortex. 1996 Apr;6(2):81–92.

31. van Lier H, Coenen AML, Drinkenburg WHIM. Behavioral transitions modulate hippocampal electroencephalogram correlates of open field behavior in the rat: support for a sensorimotor function of hippocampal rhythmical synchronous activity. J Neurosci. 2003 Mar 15;23(6):2459–65.

32. Demanuele C, James CJ, Sonuga-Barke EJ. Distinguishing low frequency oscillations within the 1/f spectral behaviour of electromagnetic brain signals. Behav Brain Funct. 2007 Dec 10;3:62.

33. Donoghue T, Haller M, Peterson EJ, Varma P, Sebastian P, Gao R, et al. Parameterizing neural power spectra into periodic and aperiodic components. Nat Neurosci. 2020 Dec;23(12):1655–65.

34. He X, Li J, Zhou G, Yang J, McKenzie S, Li Y, et al. Gating of hippocampal rhythms and memory by synaptic plasticity in inhibitory interneurons. Neuron. 2021 Mar 17;109(6):1013-1028.e9.

35. McDonnell MD, Ward LM. The benefits of noise in neural systems: bridging theory and experiment. Nat Rev Neurosci. 2011 Jun 20;12(7):415–26.

36. Tort ABL, Kramer MA, Thorn C, Gibson DJ, Kubota Y, Graybiel AM, et al. Dynamic cross-frequency couplings of local field potential oscillations in rat striatum and hippocampus during performance of a T-maze task. Proc Natl Acad Sci USA. 2008 Dec 23;105(51):20517–22.

37. Belluscio MA, Mizuseki K, Schmidt R, Kempter R, Buzsáki G. Cross-frequency phase-phase coupling between θ and γ oscillations in the hippocampus. J Neurosci. 2012 Jan 11;32(2):423–35.

38. Buzsáki G, Buhl DL, Harris KD, Csicsvari J, Czéh B, Morozov A. Hippocampal network patterns of activity in the mouse. Neuroscience. 2003;116(1):201–11.

39. Zhou Y, Sheremet A, Qin Y, Kennedy JP, DiCola NM, Burke SN, et al. Methodological considerations on the use of different spectral decomposition algorithms to study hippocampal rhythms. eNeuro. 2019 Aug 1;6(4).

40. Kovach CK, Oya H, Kawasaki H. The bispectrum and its relationship to phase-amplitude coupling. Neuroimage. 2018 Feb 23;173:518–39.

41. Hyafil A. Misidentifications of specific forms of cross-frequency coupling: three warnings. Front Neurosci. 2015 Oct 9;9:370.

42. Giehl J, Noury N, Siegel M. Dissociating harmonic and non-harmonic phase-amplitude coupling in the human brain. Neuroimage. 2021 Feb 15;227:117648.

43. Jones SR. When brain rhythms aren't "rhythmic": implication for their mechanisms and meaning. Curr Opin Neurobiol. 2016 Oct;40:72–80.

44. Scheffer-Teixeira R, Tort AB. On cross-frequency phase-phase coupling between theta and gamma oscillations in the hippocampus. eLife. 2016 Dec 7;5.

45. Oliva A, Fernández-Ruiz A, Fermino de Oliveira E, Buzsáki G. Origin of Gamma Frequency Power during Hippocampal Sharp-Wave Ripples. Cell Rep. 2018 Nov 13;25(7):1693-1700.e4.

46. Cox R, Rüber T, Staresina BP, Fell J. Heterogeneous profiles of coupled sleep oscillations in human hippocampus. Neuroimage. 2019 Nov 15;202:116178.

47. Pesaran B, Vinck M, Einevoll GT, Sirota A, Fries P, Siegel M, et al. Investigating large-scale brain dynamics using field potential recordings: analysis and interpretation. Nat Neurosci. 2018 Jul;21(7):903–19.

48. Herweg NA, Solomon EA, Kahana MJ. Theta oscillations in human memory. Trends Cogn Sci (Regul Ed). 2020 Feb 3;24(3):208–27.

49. Vinck M, van Wingerden M, Womelsdorf T, Fries P, Pennartz CMA. The pairwise phase consistency: a bias-free measure of rhythmic neuronal synchronization. Neuroimage. 2010 May 15;51(1):112–22.

50. Cacucci F, Lever C, Wills TJ, Burgess N, O'Keefe J. Theta-modulated place-by-direction cells in the hippocampal formation in the rat. J Neurosci. 2004 Sep 22;24(38):8265–77.

51. O'Keefe J, Recce ML. Phase relationship between hippocampal place units and the EEG theta rhythm. Hippocampus. 1993 Jul;3(3):317–30.

52. Royer S, Sirota A, Patel J, Buzsáki G. Distinct representations and theta dynamics in dorsal and ventral hippocampus. J Neurosci. 2010 Feb 3;30(5):1777–87.

53. Qasim SE, Fried I, Jacobs J. Phase precession in the human hippocampus and entorhinal cortex. Cell. 2021 Jun 10;184(12):3242-3255.e10.

54. Goutagny R, Jackson J, Williams S. Self-generated theta oscillations in the hippocampus. Nat Neurosci. 2009 Dec;12(12):1491–3.

55. Pignatelli M, Beyeler A, Leinekugel X. Neural circuits underlying the generation of theta oscillations. J Physiol Paris. 2012 Aug;106(3–4):81–92.

56. Bland BH. The physiology and pharmacology of hippocampal formation theta rhythms. Prog Neurobiol. 1986;26(1):1–54.

57. Yartsev MM, Witter MP, Ulanovsky N. Grid cells without theta oscillations in the entorhinal cortex of bats. Nature. 2011 Nov 2;479(7371):103–7.

58. M Aghajan Z, Schuette P, Fields TA, Tran ME, Siddiqui SM, Hasulak NR, et al. Theta Oscillations in the Human Medial Temporal Lobe during Real-World Ambulatory Movement. Curr Biol. 2017 Dec 18;27(24):3743-3751.e3.

59. Watrous AJ, Fried I, Ekstrom AD. Behavioral correlates of human hippocampal delta and theta oscillations during navigation. J Neurophysiol. 2011 Apr;105(4):1747–55.

60. Mao D, Avila E, Caziot B, Laurens J, Dickman JD, Angelaki DE. Spatial modulation of hippocampal activity in freely moving macaques. Neuron. 2021 Nov 3;109(21):3521-3534.e6.

61. Girardeau G, Lopes-Dos-Santos V. Brain neural patterns and the memory function of sleep. Science. 2021 Oct 29;374(6567):560–4.

62. Robinson TE, Kramis RC, Vanderwolf CH. Two types of cerebral activation during active sleep: relations to behavior. Brain Res. 1977 Apr 1;124(3):544–9.

63. Buzsáki G. Two-stage model of memory trace formation: a role for "noisy" brain states. Neuroscience. 1989;31(3):551–70.

64. Takeuchi S, Mima T, Murai R, Shimazu H, Isomura Y, Tsujimoto T. Gamma Oscillations and Their Cross-frequency Coupling in the Primate Hippocampus during Sleep. Sleep. 2015 Jul 1;38(7):1085–91.

65. Uchida S, Maehara T, Hirai N, Okubo Y, Shimizu H. Cortical oscillations in human medial temporal lobe during wakefulness and all-night sleep. Brain Res. 2001 Feb 9;891(1–2):7–19.

66. Cantero JL, Atienza M, Stickgold R, Kahana MJ, Madsen JR, Kocsis B. Sleep-dependent theta oscillations in the human hippocampus and neocortex. J Neurosci. 2003 Nov 26;23(34):10897–903.

67. Bódizs R, Kántor S, Szabó G, Szûcs A, Erõss L, Halász P. Rhythmic hippocampal slow oscillation characterizes REM sleep in humans. Hippocampus. 2001;11(6):747–53.

68. López-Madrona VJ, Pérez-Montoyo E, Álvarez-Salvado E, Moratal D, Herreras O, Pereda E, et al. Different theta frameworks coexist in the rat hippocampus and are coordinated during memory-guided and novelty tasks. eLife. 2020 Jul 20;9.

69. Pedrosa R, Battaglia F. Combining cortical voltage imaging and hippocampal electrophysiology for investigating global, multi-time scale activity interactions in the brain. arXiv. 2021 Dec 6;

70. Montefusco-Siegmund R, Leonard TK, Hoffman KL. Hippocampal gamma-band Synchrony and pupillary responses index memory during visual search. Hippocampus. 2017 Feb 17;27(4):425–34.

71. Chau VL, Murphy EF, Rosenbaum RS, Ryan JD, Hoffman KL. A Flicker Change Detection Task Reveals Object-in-Scene Memory Across Species. Front Behav Neurosci. 2011 Sep 20;5:58.

72. Masimore B, Kakalios J, Redish AD. Measuring fundamental frequencies in local field potentials. J Neurosci Methods. 2004 Sep 30;138(1–2):97–105.

73. Thammasan N, Miyakoshi M. Cross-Frequency Power-Power Coupling Analysis: A Useful Cross-Frequency Measure to Classify ICA-Decomposed EEG. Sensors. 2020 Dec 9;20(24).

74. Bullock TH, Achimowicz JZ, Duckrow RB, Spencer SS, Iragui-Madoz VJ. Bicoherence of intracranial EEG in sleep, wakefulness and seizures. Electroencephalogr Clin Neurophysiol. 1997 Dec;103(6):661–78.

75. Sheremet A, Burke SN, Maurer AP. Movement enhances the nonlinearity of hippocampal theta. J Neurosci. 2016 Apr 13;36(15):4218–30.

76. Torrence C, Compo GP. A practical guide to wavelet analysis. Bull Amer Meteor Soc. 1998 Jan;79(1):61–78.

77. Bédard C, Destexhe A. Macroscopic models of local field potentials and the apparent 1/f noise in brain activity. Biophys J. 2009 Apr 8;96(7):2589–603.